

# Synthesis of silicate-bridged SnO<sub>2</sub>/BiVO<sub>4</sub> nanoplate heterojunctions as efficient photocatalysts to convert CO<sub>2</sub> and degrade 2,4-dichlorophenol

*Kang Hu<sup>1</sup>, Zhijun Li<sup>1</sup>, Shuangying Chen<sup>1</sup>, Ji Bian<sup>1</sup>, Yang Qu<sup>1</sup>, Junwang Tang<sup>2,\*</sup>,  
Liqiang Jing<sup>1,\*</sup>*

<sup>1</sup>Key Laboratory of Functional Inorganic Materials Chemistry, Heilongjiang University, Ministry of Education, School of Chemistry and Materials Science, International Joint Research Center for Catalytic Technology, Harbin 150080, P. R. China. Email: [jinglq@hlju.edu.cn](mailto:jinglq@hlju.edu.cn) (L. Jing)

<sup>2</sup>Department of Chemical Engineering, University College London, Torrington Place, London WC1E 7JE, U.K. Email: [junwang.tang@ucl.ac.uk](mailto:junwang.tang@ucl.ac.uk) (J. Tang)

**Keywords:** BiVO<sub>4</sub> nanoplate, coupling SnO<sub>2</sub>, silicate bridge, charge transfer and separation, visible-light photocatalysis

**Abstract:** Bismuth vanadate (BiVO<sub>4</sub>) is a potential visible-light driven photocatalyst, and it is highly desired to greatly improve its photocatalytic activities by increasing the surface area and enhancing the utilization of high-energy-level excited electrons. In this work, BiVO<sub>4</sub> nanoplates with large specific surface area have been successfully fabricated by a hydrothermal conversion process from the pre-prepared BiOCl nanosheets. Further, the photogenerated charge separation of resulting BiVO<sub>4</sub> nanoplates has been enhanced after coupling with nanocrystalline SnO<sub>2</sub>, along with the prolonged charge lifetimes, especially for the silicate-bridged SnO<sub>2</sub>/BiVO<sub>4</sub> ones,

mainly based on the measurements of steady-state- and time-resolved- surface photovoltage responses and produced hydroxyl radical amounts. Interestingly, the amount-optimized nanocomposite exhibits exceptional visible-light photocatalytic activities, ~ 7-time and 4-time enhancements for CO<sub>2</sub> conversion to CH<sub>4</sub> and for 2,4-dichlorophenol degradation compared to pure BiVO<sub>4</sub> nanoparticles. Moreover, it has been deduced by means of designed photoelectrochemical experiments that the introduced SnO<sub>2</sub> as the proper-energy platform that can accept the visible-light-excited electrons of BiVO<sub>4</sub> nanoplates. The built silicate bridges further promote the electron transfer between them. This work opens up a new feasible route to synthesize visible-light-driven high-activity BiVO<sub>4</sub>-based nanojunction for efficient fuel production and environmental remediation.

## **1. Introduction**

The growth of human population, urbanization and rising living standards and rapid consumption of fossil fuels, such as natural gas, coal and petroleum, have greatly increased the worldwide green energy demand and brought about environmental pollution.<sup>[1,2]</sup> The extensive utilization of fossil fuels have caused huge CO<sub>2</sub> emission which has caused adverse global environmental changes.<sup>[3,4]</sup> Moreover, some highly toxic organic pollutants like chlorophenols, which are widely applied in the manufacturing process of dyes, bactericides, pesticides and wood preservatives, are harmful to organisms and environment, even at low concentration and have been listed as the top priority pollutants by the United States Environmental Protection

Agency.<sup>[5, 6]</sup> Among them, 2,4-dichlorophenol (2,4-DCP) is a very hazardous colorless organic pollutant which has attracted tremendous scientific attention as it is highly stable and has a potential carcinogenic risk to both human beings and environment.<sup>[7-9]</sup> Thus, it is very urgent and meaningful to remove 2,4-DCP from water for maintaining the security of drinking water. However, there is so far no universal solution to solve these critical issues.<sup>[10, 11]</sup> Based on these reality-problems, semiconductor photocatalysis is considered as a potential technique to convert CO<sub>2</sub>, produce H<sub>2</sub> and degrade pollutants for solving those issues due to its low cost, environmental friendliness and sustainability, etc,<sup>[12-14]</sup> compared with other traditional techniques, such as biological and electrocatalytic techniques.<sup>[15, 16]</sup>

Semiconductor with the function of absorbing light and producing electrons and holes is the key of photocatalysis. TiO<sub>2</sub> is a well-recognized photocatalyst due to its high activity and stability. However, its wide bandgap (3.2 eV for anatase) can only utilize a few percent of the solar light energy (ca. 4%). Based on the large proportion of visible light (ca. 46%) in the solar spectrum, efforts are directed towards the development of visible-light responsible photocatalysts to maximally utilize solar energy.<sup>[17-18]</sup> BiVO<sub>4</sub> is a promising photocatalyst which has inspired a great deal of interest because of its high stability, low toxicity and good visible-light photoactivity in water oxidation, pollutant degradation and so on.<sup>[19-21]</sup> However, the photocatalytic performance for BiVO<sub>4</sub> is still unsatisfied due to its very small surface area and fast charge recombination. Although efforts have been done for controlling the multifarious morphologies, such as nanoribbons, decahedrons, spheres and hollow

structure in olive shape, the resulting surface area of BiVO<sub>4</sub> is still very low, leading to the limited improvement of the photocatalytic performance of BiVO<sub>4</sub>.<sup>[22-26]</sup>

Two-dimensional (2D) nanomaterials possess large surface area to facilitate more effective adsorption, consequently improving the photocatalytic performance.<sup>[27]</sup> Furthermore, 2D nanomaterials favors electron transfer due to the very short electron diffusion path, mitigating charge recombination. Hence, it is highly desired to prepare 2D BiVO<sub>4</sub> nano-photocatalyst with large specific surface area. However, different from other bismuth based oxides such as bismuth oxyhalides and bismuth tungstate, 2D BiVO<sub>4</sub> is hard to directly prepare due to the special crystal structure.<sup>[28]</sup> Thus, it is urgently required to find a new path to prepare 2D BiVO<sub>4</sub> nanomaterial. recently, Kyoung-Shin Choi et al prepared high-photochemical-activity nanoporous BiVO<sub>4</sub> electrode by annealing BiOI and vanadium precursor in air.<sup>[29]</sup> Very recently, we have found that BiOCl was unstable due to the easily released Cl<sup>-</sup>, which could be substituted by other anion groups,<sup>[30]</sup> and 2D BiOCl nanosheets were easily prepared.<sup>[31]</sup> Therefore, a fancy that applying BiOCl nanosheets as a precursor to prepare 2D BiVO<sub>4</sub> nano-photocatalyst with large specific surface area through ion exchange is proposed which has not yet been reported.

It is naturally expected to develop a feasible strategy for solving the poor charge separation which as mentioned above is another reason for the low photocatalytic performance of BiVO<sub>4</sub>.<sup>[32]</sup> Based on our previous works, coupling with wide bandgap semiconductors like TiO<sub>2</sub> or ZnO as an appropriate platform for accepting the high-energy electrons generated in BiVO<sub>4</sub> under visible-light irradiation, so as to

improve the charge separation and prolong their lifetimes.<sup>[33, 34]</sup> Moreover, it was confirmed that coupled SnO<sub>2</sub> could accept more photogenerated electrons from Fe<sub>2</sub>O<sub>3</sub> compared to the coupled TiO<sub>2</sub> or ZnO in the composite, due to the more suitable conduction band position.<sup>[35]</sup> So a rational design is to couple SnO<sub>2</sub> with BiVO<sub>4</sub> for improving the charge separation and prolonging the charge lifetimes, so as to further promote the photocatalytic performance. In addition, the quality of interfacial contact between semiconductors deeply affects the charge transfer in heterojunctional nanocomposites. Owing to the mismatched crystal lattice between BiVO<sub>4</sub> and SnO<sub>2</sub>, it's highly essential to build an electron transferring buffer like silicate bridges to promote the charge transfer.<sup>[34]</sup>

In this study, 2D BiVO<sub>4</sub> nanoplates were prepared via a hydrothermal ion exchange process from BiOCl nanosheets. The as-prepared 2D BiVO<sub>4</sub> nanoplates exhibit much larger surface area compared to BiVO<sub>4</sub> nanoparticles, so has a potential to enhance photocatalytic property. It has then been demonstrated by steady-state surface photovoltage spectroscopy (SS-SPS) and transient-state surface photovoltage (TS-SPV) that the charge separation and lifetime could be further improved by coupling a proper amount of SnO<sub>2</sub> as an electron accepting platform, in particular the optimal silicate-bridged one. This has been illustrated by the promoted photocatalytic activities of CO<sub>2</sub> conversion and 2,4-DCP degradation under visible-light irradiation. This work is further valuable for synthesizing 2D visible-light-driven BiVO<sub>4</sub>-based nanophotocatalysts for both high efficient solar fuel production and environmental remediation.

## 2. Results and Discussion

### 2.1. Structural characterization of BiVO<sub>4</sub> nanoplates

2D BiVO<sub>4</sub> nanoplates were prepared via hydrothermal ion exchange process from BiOCl nanosheets. The X-ray diffraction (XRD) patterns (Figure S1A, Supporting Information) of BV-NP3 (BV-NP is BiVO<sub>4</sub> nanoplate, and 3 represents the hydrothermal time of 3 h) sample exhibit two diffraction peaks at 2θ of 25.9° and 32.5°, which are identified as the main peaks of the remnant BiOCl phase (JCPDS card number 85-0861), suggesting that BiOCl has not yet been fully transformed because of short hydrothermal time. But no characteristic peaks of any other phases and impurities are observed over BV-NP6 and BV-NP9 samples, indicating the high purity of the BiVO<sub>4</sub> nanoplates and BiOCl nanosheets could be completely converted to BiVO<sub>4</sub> nanoplates through the hydrothermal process. It is evident from ultraviolet visible (UV-vis) diffuse reflection spectrum (DRS) (Figure S1B, Supporting Information) that the bandgap of prepared BiVO<sub>4</sub> nanoplates is ~ 2.2 eV according to the widely accepted energy bandgap equation:  $E_g = 1240/\lambda$ , where  $E_g$  is the energy bandgap.<sup>[36]</sup> Moreover, as shown from scanning electron micrograph (SEM) images (**Figure 1A**) of the BV-NP6 photocatalyst, it is indicated that the prepared monoclinic BiVO<sub>4</sub> (JCPDS card number 83-1699) is plate-like with 150-200 nm in width and 30-40 nm in thickness, which copies the 2D structure of BiOCl precursor (see SEM image in Figure S2A, Supporting Information). BiVO<sub>4</sub> nanoparticles were also prepared for comparison and its SEM image shows in Figure S2B (Supporting Information). Transmission electron microscopy (TEM) image and high-resolution

transmission electron microscopy (HRTEM) image as shown in Figure S3 (Supporting Information) further confirm the 2D plate-like structure, and the fringe spacing of 0.26 nm agrees well with the spacing of the (200) lattice plane of monoclinic BiVO<sub>4</sub>.<sup>[28]</sup> These results clearly demonstrate the successful preparation of 2D BiVO<sub>4</sub> nanoplates.

Moreover, the nitrogen adsorption-desorption isotherms (Figure S4, Supporting Information) show BV-NP6 with a large BET surface area of 11.6 m<sup>2</sup> g<sup>-1</sup> is the optimal one which is 10-time larger than the BiVO<sub>4</sub> nanoparticles (1.1 m<sup>2</sup> g<sup>-1</sup>). The fluorescence spectrum (FS) of the formed hydroxyl radicals (•OH) in **Figure 1B** indicates that BV-NP6 displays a higher efficient charge separation compared to BiVO<sub>4</sub> nanoparticles.<sup>[37]</sup> **Figure 1C, D** show the visible-light photocatalytic activities of BiVO<sub>4</sub> nanoparticles and BV-NP6 samples for CO<sub>2</sub> reduction and 2,4-DCP degradation. It is shown that the BV-NP6 displays much higher photoactivities compared with BiVO<sub>4</sub> nanoparticles under visible-light irradiation which are in agreement with the corresponding amount of produced •OH. Thus, it is concluded that the plate-like structure with large specific surface area could be very favorable for improving the photocatalytic performance of BiVO<sub>4</sub>.

## 2.2. Effect of coupling with SnO<sub>2</sub>

In order to further improve the photogenerated charge separation of BV-NP6, SnO<sub>2</sub> with different amounts are coupled. The XRD patterns and UV-vis DRS spectra of YS/BV-NP6 (S means SnO<sub>2</sub>, and Y represents the different percentage mole ratios of SnO<sub>2</sub> coupled to BiVO<sub>4</sub>) in Figure S5 (Supporting Information) clearly indicate that

the phase compositions and optical absorbance of BV-NP6 remain unchanged after coupling with different amount of SnO<sub>2</sub> nanoparticles. In addition, the diffraction peaks assigned to the monoclinic phase of BiVO<sub>4</sub> are accompanied by the characteristic peaks indexed to the tetragonal SnO<sub>2</sub> (JCPDS card number 77-0447). No additional impurity phase was found in the diffraction patterns, suggesting that the SnO<sub>2</sub>/BiVO<sub>4</sub> composites exhibit the coexistence of both BiVO<sub>4</sub> and SnO<sub>2</sub> phases. Furthermore, as the amount of SnO<sub>2</sub> increases in the SnO<sub>2</sub>/BiVO<sub>4</sub> composites, the intensity of (110) peak of the tetragonal-phase SnO<sub>2</sub> is gradually increased.

The visible-light photocatalytic activities of BV-NP6 and YS/BV-NP6 samples were evaluated for CO<sub>2</sub> reduction to CH<sub>4</sub> as shown in **Figure 2A**. It is clear that BV-NP6 sample exhibits obvious photocatalytic performance for CO<sub>2</sub> conversion to CH<sub>4</sub> (1.1 μmol g<sup>-1</sup> h<sup>-1</sup>). However, the photocatalytic activities are greatly improved for YS/BV-NP6 samples especially for the amount-optimized 10S/BV-NP6 one (1.7 μmol g<sup>-1</sup> h<sup>-1</sup>) which is ~ 4-time higher than BiVO<sub>4</sub> nanoparticles (0.4 μmol g<sup>-1</sup> h<sup>-1</sup>). To further investigate the photoactivities of the as prepared samples, we measured the visible-light photocatalytic performance of BV-NP6 and YS/BV-NP6 samples for 2,4-DCP degradation as shown in **Figure 2B**. It is clear that the photocatalytic activities of BiVO<sub>4</sub> nanoplates for 2,4-DCP degradation are greatly improved after coupling with SnO<sub>2</sub>. Interestingly, 10S/BV-NP6 sample exhibits the highest photoactivity for 2,4-DCP degradation (72.2 %) among all samples which is about 3 times higher compared to BiVO<sub>4</sub> nanoparticles (24.2 %). This is consistent with the above photocatalytic activities for CO<sub>2</sub> reduction. The improved photocatalytic

activities are attributed to the promoted photogenerated charge separation after coupling SnO<sub>2</sub>, mainly based on the produced •OH amount analysis and the observed SS-SPS responses in air as shown in **Figure 2C**, since a strong SS-SPS response usually corresponds to high charge separation. In addition, to confirm the enhanced charge separation, we measured the photoelectrochemical (PEC) behaviors under visible-light irradiation in 1.0 M NaOH solution as shown in **Figure 2D**. It is obvious that the photocurrent density of BiVO<sub>4</sub> film is very low. However, as the amount of introduced SnO<sub>2</sub> further increases, the corresponding photocurrent density is gradually enhanced. The value of the 10S/BV-NP6 film is the largest among the nanocomposite films by about 2-time compared with the BV-NP6 at the applied voltage of 0.4 V. This indicates that coupling a proper amount of nanocrystalline SnO<sub>2</sub> is favorable to enhance the photocatalytic properties of BiVO<sub>4</sub>.

### **2.3. Effect of introduced silicate bridges**

It is meaningful to improve the connection by using silicate bridges between BiVO<sub>4</sub> and SnO<sub>2</sub> due to their mismatched lattice parameters. On the basis of XRD patterns and UV-vis DRS spectra of 10S/BV-NP6 and ZSi-10S/BV-NP6 (Si means TEOS, and Z represents the mole ratios percentage of TEOS to SnO<sub>2</sub>) samples as shown in Figure S6A, B (Supporting Information), it is suggested that the phase compositions and band edges are unchanged after introducing silicate groups. In addition, the area-selected HRTEM images as shown in **Figure 3A, B**, well confirm the junctions between BiVO<sub>4</sub> and SnO<sub>2</sub>, indicating that the nano-SnO<sub>2</sub> is successfully coupled. Moreover, the morphology and size are unchanged after coupling with

silicate-bridged SnO<sub>2</sub>. Importantly, from X-ray photoelectron spectroscopy (XPS) as shown in **Figure 4** and Figure S7 (Supporting Information), it is observed that the Si 2p (~ 133.6 eV) peak of 5Si-10S/BV-NP6 is characteristic of silicate groups, which is in good agreement with a previous report on silicate electron-bridging between BiVO<sub>4</sub> and ZnO.<sup>[34]</sup> According to the fourier-transform infrared (FT-IR) spectra as shown in the inset of Figure 4 and Figure S8 (Supporting Information), it is confirmed that there are some peaks at the wavenumber of 1080-1105 cm<sup>-1</sup> assigned to the asymmetric vibration of Si-O-Si and 940-960 cm<sup>-1</sup> for the Si-OH vibration over the silicate-bridged nanocomposites,<sup>[38]</sup> and the corresponding absorption peak intensity is gradually increased as the amount of introduced silicate groups becomes large. From both XPS analyses and FT-IR, it is demonstrated that Si exists in the form of silicate group on the interface of BiVO<sub>4</sub> and SnO<sub>2</sub>.

The photocatalytic activities of 10S/BV-NP6 and ZSi-10S/BV-NP6 samples were evaluated for CO<sub>2</sub> reduction under visible-light irradiation as shown in **Figure 5A**. Interestingly, this obviously suggests that the visible-light activities of ZSi-10S/BV-NP6 nanocomposites for CO<sub>2</sub> conversion are greatly improved compared to non-silicate-bridged one (10S/BV-NP6) and the amount-optimized 5Si-10S/BV-NP6 sample exhibits the highest photocatalytic performance for CO<sub>2</sub> conversion to CH<sub>4</sub> (3.3 μmol g<sup>-1</sup> h<sup>-1</sup>) under visible-light irradiation. It is confirmed that 5Si-10S/BV-NP6 sample exhibits about 2 times and 7 times enhanced visible-light activity for CO<sub>2</sub> conversion to CH<sub>4</sub> compared to the 10S/BV-NP6 and BiVO<sub>4</sub> nanoparticles, respectively. Moreover, the silicate-bridged samples display

enhanced visible-light photocatalytic activities for 2,4-DCP degradation as shown in **Figure 5B**, among which 5Si-10S/BV-NP6 with the optimal silicate amount shows the highest photoactivity with an approximately 71 % (about 4 times) and 23 % enhancement compared to BiVO<sub>4</sub> nanoparticles and 10S/BV-NP6 nanocomposite, respectively. These enhanced photoactivities are supported by the formed •OH radical amount and the observed SS-SPS response in air as shown in **Figure 5C**, indicating obviously enhanced charge separation of 5Si-10S/BV-NP6. As shown in **Figure 5D**, the PEC measurements provide further evidence that the photocurrent density of resulting 10S/BV-NP6 film is gradually enhanced after introducing silicate bridges. The value of the 5Si-10S/BV-NP6 film is the largest among the nanocomposite films by about 3-time and 1.5-time compared with the BV-NP6 and 10S/BV-NP6 respectively at the applied voltage of 0.4 V. Moreover, the electrochemical impedance spectra (EIS) Nyquist plots as shown in Figure S9 (Supporting Information) provide further evidences that the silicate-bridged sample (5Si-10S/BV-NP6) displays the smallest arc radii compared to those without any modifications (BV-NP6 and 10S/BV-NP6), suggesting the reduced interfacial transmission resistance after silicate bridging.<sup>[39]</sup> Thus, it is deduced that silicate bridges between SnO<sub>2</sub> and BiVO<sub>4</sub> are built effectively, and these would be much favorable for the spatial transfer of photogenerated charges. Furthermore, the amount of O<sub>2</sub> produced by H<sub>2</sub>O oxidation during CO<sub>2</sub> conversion as shown in Figure S10 (Supporting Information), it is clear that the visible-light photocatalytic activities of BiVO<sub>4</sub> nanoplates is greatly improved after coupling a proper amount of SnO<sub>2</sub>. Interestingly, it is noticed that after further

introducing optimal-amount silicate, the photocatalytic activity for O<sub>2</sub> evolution is remarkably improved and the highest photoactivity is observed for 5Si-10S/BV-NP6 nanocomposite (7.2 μmol g<sup>-1</sup> h<sup>-1</sup>) which exhibits about 2 times and 7 times enhanced photoactivities compared to the un-bridged 10S/BV-NP6 one (3.7 μmol g<sup>-1</sup> h<sup>-1</sup>) and BiVO<sub>4</sub> nanoparticles (1.2 μmol g<sup>-1</sup> h<sup>-1</sup>), respectively, corresponding to the activities for CO<sub>2</sub> conversion to CH<sub>4</sub>. Since the stability of photocatalysts plays an important role in evaluating the photocatalytic performance, recyclability of 5Si-10S/BV-NP6 for CO<sub>2</sub> conversion and 2,4-DCP degradation were measured as shown in Figure S11 (Supporting Information). It can be seen that no inactivation is observed even after 4 runs in 24 h and 8 h respectively, indicating that 5Si-10S/BV-NP6 is highly stable during the whole photocatalytic processes. In addition, the radicals and hole trapping experiments (Figure S12, Supporting Information) are applied to elucidate the photocatalytic degradation processes of BV-NP6, 10S/BV-NP6 and 5Si-10S/BV-NP6. EDTA-2Na, isopropyl alcohol (IPA), and benzoquinone (BQ) are used to scavenge h<sup>+</sup>, •OH and •O<sub>2</sub><sup>-</sup>, respectively. When IPA is added to the photocatalytic system, the photoactivity of BV-NP6 is obviously decreased, indicating that the photogenerated •OH is dominant in the degradation of 2,4-DCP, but the formed •O<sub>2</sub><sup>-</sup> becomes the dominant active species over 10S/BV-NP6 and 5Si-10S/BV-NP6 samples. Thus, it is confirmed that the visible-light photocatalytic performance of BiVO<sub>4</sub> could be greatly enhanced by coupling silicate bridged SnO<sub>2</sub>.

#### **2.4. Mechanism for photogenerated charge transfer and separation**

SS-SPS and TS-SPV responses are known as effective methods to investigate the

photogenerated charge properties of semiconducting solid materials.<sup>[40]</sup> It is clear that 5Si-10S/BV-NP6 exhibits a detectable SS-SPS response in N<sub>2</sub> as shown in **Figure 6A** and Figure S13 (Supporting Information), much higher than 10S/BV-NP6. The detected SS-SPS response in N<sub>2</sub> should be attributed to the spatial transfer of photogenerated energetic electrons from BiVO<sub>4</sub> to SnO<sub>2</sub>, according to the fundamental of SS-SPS and previous work.<sup>[33]</sup> By comparison, it is suggested that the silicate bridges are favorable to transport charge and promote electron transfer, this can be attributed to the silicate bridges acting as a favorable charge transport channel in the fabricated nanocomposite. To further explore the properties of photogenerated charges, TS-SPV was used to investigate the dynamic processes of the photogenerated charge carriers. According to the TS-SPV responses as shown in **Figure 6B**, it is noticed that the 5Si-10S/BV-NP6 nanocomposite exhibits the strongest TS-SPV responses in air under laser pulse irradiation with 532 nm, especially with the obviously-prolonged carrier lifetime by ~ ms compared with 10S/BV-NP6 and BV-NP6, corresponding to the high visible-light-excited photogenerated charge separation. This also verifies the above results of SS-SPS responses.

On the basis of the above analyses, it is confirmed that the introduction of silicate-bridged SnO<sub>2</sub> promotes the separation prolongs and the lifetime of photogenerated charges, leading to the highly improved visible-light activities for CO<sub>2</sub> reduction and 2,4-DCP degradation. It is assumed that the charge separation enhancement is attributed to the transfer of electrons from BiVO<sub>4</sub> to

SnO<sub>2</sub> through silicate bridging in the fabricated nanocomposites. To further verify this charge transfer mechanism, the photocurrent action spectra of BV-NP6, 10S/BV-NP6 and 5Si-10S/BV-NP6 with different wavelength modulations were obtained as shown in **Figure 7A**. A weak photocurrent is observed at ~ 560 nm, resulting from the photo-excited BiVO<sub>4</sub> with a bandgap of 2.2 eV. Noticeably, the photocurrents for all the three catalysts are obviously increased below 560 nm, which corresponds to the minimum energy difference between the valence band (VB) top and conduction band (CB) bottom of BiVO<sub>4</sub> for producing electrons. In particular, the silicate-bridged one exhibits the largest photocurrent. A possible mechanism schematic is depicted in **Figure 7B**, BiVO<sub>4</sub> absorbs visible light photons and generate electron-hole pairs. The charge separation enhancement mainly results from the transformation of electrons from the CB of BiVO<sub>4</sub> to SnO<sub>2</sub>, through the silicate-bridges. Because the bottom of the CB stands at about 0 eV vs. normal hydrogen electrode (NHE), it is deduced that the top of its VB is located at 2.2 eV. Thus, the energy difference between the BiVO<sub>4</sub> VB top and SnO<sub>2</sub> CB bottom (0 eV) is 2.2 eV, corresponding to the light energy of about 564 nm which can be calculated by the equation:  $\lambda = 1240/E_g$ , indicating that the photogenerated electrons of BiVO<sub>4</sub> below 564 nm are allowed energetically to transfer to SnO<sub>2</sub> in space, and the highest energy level of visible-light-excited electrons (by the light of 400 nm) would reach -0.9 eV. This is consistent with the above-mentioned results of photocurrent action spectra. Hence, it is suggested that the visible light in the wavelength range from

564 to 400 nm, is favored for visible-light-excited electrons transfer. Therefore, it is deduced that the increased charge separation is ascribed to the coupled SnO<sub>2</sub> as the suitable electron energy platform and the introduced silicate bridges as the charge transport pathway, and this also verifies our previous prediction that there is greater potential for solar energy utilization by the fabricated nanocomposite in the visible-light region compared to TiO<sub>2</sub>/BiVO<sub>4</sub> nanocomposite (or ZnO/BiVO<sub>4</sub> nanocomposite).

### **3. Conclusions**

In summary, BiVO<sub>4</sub> nanoplates with large specific surface area were successfully fabricated by a hydrothermal conversion method by using BiOCl nanosheets as precursors. It was confirmed by TS-SPV responses, SS-SPS, and PEC measurements that coupling a proper amount of SnO<sub>2</sub> could dramatically prolong the carrier lifetime and promote the charge separation, leading to superior performance for CO<sub>2</sub> conversion and 2,4-DCP decomposition. Further, the silicate bridges between BiVO<sub>4</sub> and SnO<sub>2</sub> were successfully fabricated so that the visible-light-excited photogenerated electrons transfer across the heterogeneous interface has been greatly improved, so as to further prolonging the lifetime due to promoting the separation of photogenerated charges. As a consequence, the fabricated 2D silicate-bridged SnO<sub>2</sub>/BiVO<sub>4</sub> nanocomposites exhibited much higher photocatalytic activities for CO<sub>2</sub> conversion, e.g. even 7 times and for 2,4-DCP degradation by about 4 times enhancement compared to BiVO<sub>4</sub> nanoparticles. The successful development of the novel

silicate-bridged  $\text{SnO}_2/\text{BiVO}_4$  nanoplates with enhanced photocatalytic performance and acceptable stability pave a novel way to synthesize 2D bismuth-based visible-light responsive semiconductor composites for potential applications in fuels generation and environmental purification.

## **4. Experimental Section**

### **4.1. Reagents**

All chemicals and reagents were of analytical grade and used without further purification. Deionized water was used throughout the experiments.

### **4.2. Synthesis of materials**

Synthesis of  $\text{BiVO}_4$  nanoplates. In a typical synthesis, 1.0 mmol of  $\text{BiOCl}$  nanosheets were added into 100 mL of distilled water under mild stirring to get a white suspension. And then, 1.0 mmol of  $\text{NaVO}_3$  was added into the white suspension to form an orange suspension. After adjusting pH of the solution to 7.0 with the help of  $1.0 \text{ mmol L}^{-1} \text{ NH}_3 \cdot \text{H}_2\text{O}$  solution, the suspension changed into light yellow. Subsequently, it was transferred into a Teflon-lined autoclave and heated in an oven at  $160 \text{ }^\circ\text{C}$  for 3 h to 9 h, and then naturally cooled to room temperature. The yellow powders formed were washed with distilled water and ethanol several times to remove ions and possible remnants and then vacuum-dried for further characterization. The as-prepared samples were denoted by BV-NP3, BV-NP6 and BV-NP9, which agree with the corresponding hydrothermal time.

Synthesis of  $\text{SnO}_2$  nanoparticles.  $\text{SnO}_2$  nanoparticles were prepared using a typical

preparation method. 2.0 g of  $\text{SnCl}_4 \cdot 5\text{H}_2\text{O}$  was dissolved in deionized water and 1.0 mol  $\text{L}^{-1}$  NaOH solution was added dropwise under continuous stirring. At the beginning, a white cloudy suspension was formed in the acidic solution which then slowly disappeared with addition of NaOH, and became clear until the pH value reached 12.0. Subsequently, the obtained solution was transferred into a 100 mL Teflon-lined stainless-steel autoclave and hydrothermally heated at 200 °C for 12 h. After cooling to room temperature naturally, the obtained product was centrifugally washed 3 times with distilled water to remove impurities and then dried overnight at 60 °C in an oven.  $\text{SnO}_2$  nanoparticles were obtained after calcination at 450 °C for 2 h in air.

Synthesis of  $\text{SnO}_2/\text{BiVO}_4$  nanocomposites.  $\text{SnO}_2/\text{BiVO}_4$  nanocomposites were prepared by using a simple wet-chemical process. 1.0 g  $\text{BiVO}_4$  was mixed with 20 mL absolute ethanol and 5 mL  $\text{H}_2\text{O}$  and a certain amount of  $\text{SnO}_2$  was added gradually to it under stirring. Finally, the mixed solution was stirred for 1 h and dried at 80 °C, followed by calcination at 450 °C for 1 h (5 °C  $\text{min}^{-1}$ ). The as prepared samples were represented by YS/BV-NP, in which Y means the different percentage mole ratios (5, 10 and 15 %) of  $\text{SnO}_2$  to  $\text{BiVO}_4$ , S means  $\text{SnO}_2$ , and BV-NP means  $\text{BiVO}_4$  nanoplates.

Synthesis of silicate-bridged  $\text{SnO}_2/\text{BiVO}_4$  nanocomposites. 0.3 mmol  $\text{SnO}_2$  was added into a certain concentration of 20 mL TEOS alcohol solution. After stirring for 2 h, the mixture was dried at 80 °C and then annealed at 450 °C for 1 h. The obtained powders were denoted by ZSi-S. Subsequently, ZSi-S was added into the system

containing 3.0 mmol BiVO<sub>4</sub> and stirred for 1 h. The mixture was dried at 80 °C and annealed at 450 °C for 1 h. For ZSi-10S/BV-NP and ZSi-S, Z represents the different percentage mole ratios (3, 5 and 7 %) of used TEOS to SnO<sub>2</sub>.

### **4.3. Characterization**

The XRD patterns of the samples were characterized with Bruker D8 Advance X-ray diffractometer equipped with a graphite monochromatized Cu K $\alpha$  radiation ( $\lambda = 1.541874 \text{ \AA}$ ). The UV-vis DRS of the samples were recorded with a Model Shimadzu UV2550 spectrophotometer. Electron microscopy images of the samples were recorded on a JEOL JEM-2100 TEM operated at 160 kV. SEM images were taken using a Hitachi S-4800 instrument (Tokyo, Japan), operated at acceleration voltage of 15 kV. The specific surface area was determined according to the BET method using a Tristar II 3020 surface area and porosity analyzer (micromeritics). The FT-IR spectra of the samples were collected with a Bruker Equinox 55 Spectrometer, using KBr as diluents. XPS analysis were carried out using a Kratos-AXIS ULTRA DLD apparatus with Al (Mono) X-ray source, and the binding energies were calibrated with respect to the signal for adventitious carbon (binding energy = 284.6 eV).

### **4.4. SS-SPS and TS-SPV measurements**

The atmosphere-controlled SS-SPS measurements were carried out with a home-built apparatus equipped with a lock-in amplifier (SR830) and synchronized with a light chopper (SR540). The powder sample was sandwiched between two indium tin oxide (ITO) glass electrodes and the electrodes were kept in an atmosphere-controlled sealed container. Radiations from a 500 W xenon lamp (CHF XQ 500 W, Global xe

lamp power) were passed through a double prism monochromator (SBP300) to get a monochromatic light.

TS-SPV measurements were collected by the process that the sample chamber connected an ITO glass as top electrode and a steel substrate as bottom electrode, and a 10  $\mu\text{m}$  thick mica spacer was placed between the ITO glass and the sample to decrease the space charge region at the ITO-sample interface. The samples were excited by a radiation pulse of 532 nm with 10 ns width from the second harmonic of a neodymium-doped yttrium aluminum garnet (Nd: YAG) laser (Lab-130-10H, Newport, Co.). Intensity of the pulse was measured by a high-energy pyroelectric sensor (PE50BF-DIF-C, Ophir Photonics Group). The signals were amplified with a pre-amplifier and then registered by a 1.0 GHz digital phosphor oscilloscope (DPO 4104B, Tektronix). The TS-SPV measurements were performed in air atmosphere and at room temperature.

## **4.5. Evaluation of photocatalytic activities**

### *4.5.1. Evaluation of photocatalytic activities for CO<sub>2</sub> conversion*

In the photocatalytic conversion of CO<sub>2</sub>, for each experiment, 0.2 g powder sample was dispersed in H<sub>2</sub>O (5 mL) contained in a cylindrical steel reactor with 100 mL volume and area 3.5 cm<sup>2</sup>. A 300 W xenon arc lamp was used as the light source with a cut-off filter of  $\lambda > 420$  nm for the photocatalytic reaction. High purity CO<sub>2</sub> gas was passed through H<sub>2</sub>O and then entered into the reaction setup for reaching ambient pressure. The used photocatalyst was allowed to equilibrate in the CO<sub>2</sub>/H<sub>2</sub>O system for 1 h. During irradiation, 0.5 mL of gas was continually taken from the reaction cell

at given time interval for the analyses of CO and O<sub>2</sub> concentration with the help of a gas chromatograph (Tech, GC-7900 with TCD by N<sub>2</sub> gas carrier). Similarly, the amount of CH<sub>4</sub> was detected with FID (GC-2014 with Shimadzu Corp., Japan, with N<sub>2</sub> gas carrier).

#### *4.5.2. Photocatalytic activities for degrading 2,4-DCP*

The photocatalytic activities of the samples were further evaluated by degrading 2,4-DCP under visible light using a 150 W xenon lamp (GYZ220). 0.2 g powder photocatalyst and 2,4-DCP solution (50 mL, 10 mg L<sup>-1</sup>) were mixed in a 100 mL beaker under stirring. Before irradiation, the mixture was stirred in dark for 15 min to reach adsorption-desorption equilibrium and the dark concentration of 2,4-DCP was measured with Shimadzu UV-2550 spectrophotometer at the characteristic optical absorption of 285 nm. After irradiation for 2 h under visible light, a certain amount of the irradiated solution was centrifuged and the concentration of 2,4-DCP was again measured to calculate its percent degradation. Other experimental sections are shown in the Supporting Information.

### **Supporting Information**

Supporting Information is available from the Wiley Online Library or from the author.

### **Acknowledgements**

We are grateful for financial support from NSFC (U1401245, 21501052, 91622119), the Program for Innovative Research Team in Chinese Universities (IRT1237), the Research Project of Chinese Ministry of Education (213011A), and the Science Foundation for Excellent Youth of Harbin City of China (2014RFYXJ002,

2016RQQXJ099).

## References

- [1] Y. P. Yuan, L. W. Ruan, J. Barber, S. C. J. Loo, C. Xue, *Energy Environ. Sci.* **2014**, *7*, 3934.
- [2] G. Centi, E. A. Quadrelli, S. Perathoner, *Energy Environ. Sci.* **2013**, *6*, 1711.
- [3] T. Nakajima, Y. Tamaki, K. Ueno, E. Kato, T. Nishikawa, K. Ohkubo, Y. Yamazaki, T. Morimoto, O. Ishitani, *J. Am. Chem. Soc.* **2016**, *138*, 13818.
- [4] I. Shown, H. C. Hsu, Y. C. Chang, C. H. Lin, P. K. Roy, A. Ganguly, C. H. Wang, J. K. Chang, C. I. Wu, L. C. Chen, K. H. Chen, *Nano Lett.* **2014**, *14*, 6097.
- [5] R. P. Schwarzenbach, B. I. Escher, K. Fenner, T. B. Hofstetter, C. A. Johnson, U. V. Gunten, B. Wehrli, *Science* **2016**, *313*, 1072.
- [6] K. Yang, W. H. Wu, Q. F. Jing, W. Jiang, B. S. Xing, *Environ. Sci. Technol.* **2010**, *44*, 3021.
- [7] S. Chiron, C. Minero, D. Vione, *Environ. Sci. Technol.* **2007**, *41*, 3127.
- [8] J. Huang, Q. Chang, Y. Ding, X. Han, H. Tang, *Chem. Eng. J.* **2014**, *254*, 434.
- [9] A. Chen, G. Zeng, G. Chen, X. Hu, M. Yan, S. Guan, C. Shang, L. Lu, Z. Zou, G. Xie, *Chem. Eng. J.* **2012**, *191*, 85.
- [10] Y. Chen, C. W. Li, M. W. Kanan, *J. Am. Chem. Soc.* **2012**, *134*, 19969.
- [11] A. Chapovetsky, T. H. Do, R. Haiges, M. K. Takase, S. C. Marinescu, *J. Am. Chem. Soc.* **2016**, *138*, 5765.
- [12] J. W. Tang, J. R. Durrant, D. R. Klug, *J. Am. Chem. Soc.* **2008**, *130*, 13885
- [13] K. F. Li, X. Q. An, K. H. Parka, M. Khraisheh, J. W. Tang, *Catal. Today* **2014**,

224, 3.

- [14] H. Tong, S. Ouyang, Y. Bi, N. Umezawa, M. Oshikiri, J. Ye, *Adv. Mater.* **2012**, *24*, 229.
- [15] X. Chang, T. Wang, J. Gong, *Energy Environ. Sci.* **2016**, *9*, 2177.
- [16] Y. Zheng, J. Liu, J. Liang, M. Jaroniecc, S. Z. Qiao, *Energy Environ. Sci.* **2012**, *5*, 6717.
- [17] X. Chen, L. Liu, P. Y. Yu, S. S. Mao, *Science*, **2011**, *331*, 746.
- [18] A. Kachina, E. Puzenat, S. O. Chikh, C. Geantet, P. Delichere, P. Afanasiev, *Chem. Mater.* **2012**, *24*, 636.
- [19] L. Zhang, D. R. Chen, X. L. Jiao, *J. Phys. Chem. B* **2006**, *110*, 2668.
- [20] H. L. Tan, A. Suyanto, A. T. D. Denko, W. H. Saputera, R. Amal, F. E. Osterloh, Y. H. Ng, *Part. Part. Syst. Character.* **2017**, *34*, 1600290.
- [21] F. Xu, X. C. Lv, D. X. Kong, W. Y. Teoh, *Part. Part. Syst. Character.* **2017**, *34*, 1600300.
- [22] Q. Yu, Z. R. Tang, Y. J. Xu, *J. Energy Chem.* **2014**, *23*, 564.
- [23] F. X. Wang, M. W. Shao, L. Cheng, J. Hua, X. W. Wei, *Mater. Res. Bull.* **2009**, *44*, 1687.
- [24] D. E. Wang, R. G. Li, J. Zhu, J. Y. Shi, J. F. Han, X. Zong, C. Li, *J. Phys. Chem. C* **2012**, *116*, 5082.
- [25] W. Z. Yin, W. Z. Wang, L. Zhou, S. M. Sun, L. Zhang, *J. Hazard. Mater.* **2010**, *173*, 194.
- [26] M. L. Guan, D. K. Ma, S. W. Hu, Y. J. Chen, S. M. Huang, *Inorg. Chem.* **2011**, *50*,

800.

- [27] K. H. Qi, X. Q. Chen, Y. Y. Liu, J. H. Xin, C. L. Mak, W. A. Daoud, *J. Mater. Chem.* **2007**, *17*, 3504.
- [28] G. C. Xi, J. H. Ye, *Chem. Commun.* **2010**, *46*, 1893.
- [29] T. W. Kim, K. S. Choi, *Science*, **2014**, *343*, 990.
- [30] Z. J. Li, Y. Qu, K. Hu, M. Humayun, S. Y. Chen, L. Q. Jing, *Appl. Catal. B: Environ.* **2017**, *203*, 355.
- [31] J. Y. Xiong, G. Cheng, G. F. Li, F. Qin, R. Chen, *RSC Adv.* **2011**, *1*, 1542.
- [32] P. Chatchai, S. Y. Kishioka, Y. Murakami, A. Y. Nosaka, Y. Nosaka, *Electrochim. Acta.* **2010**, *55*, 592.
- [33] J. Bian, Y. Qu, F. Raziq, X. L. Zhang, N. Sun, L. Q. Jing, *J. Phys. Chem. C* **2016**, *120*, 11831.
- [34] X. D. Fu, M. Z. Xie, P. Luan, L. Q. Jing, *ACS Appl. Mater. Interfaces.* **2014**, *6*, 18550.
- [35] Z. J. Li, P. Luan, X. L. Zhang, Y. Qu, F. Raziq, J. S. Wang, L. Q. Jing, *Nano Research.* **2017**, *10*, 2321.
- [36] J. Xu, X. Li, X. Wu, W. Wang, R. Fan, X. Liu, H. Xue, *J. Phys. Chem. C* **2016**, *120*, 12666.
- [37] H. Wang, Y. Su, H. X. Zhao, H. T. Yu, S. Chen, Y. B. Zhang, X. Quan, *Environ. Sci. Technol.* **2014**, *48*, 11984.
- [38] K. Y. Jung, S. B. Park, *Appl. Catal. B: Environ.* **2000**, *25*, 249.
- [39] L. Zou, H. Wang, X. Wang, *ACS Sustainable Chem. Eng.* **2017**, *5*, 303.

**Figures:**

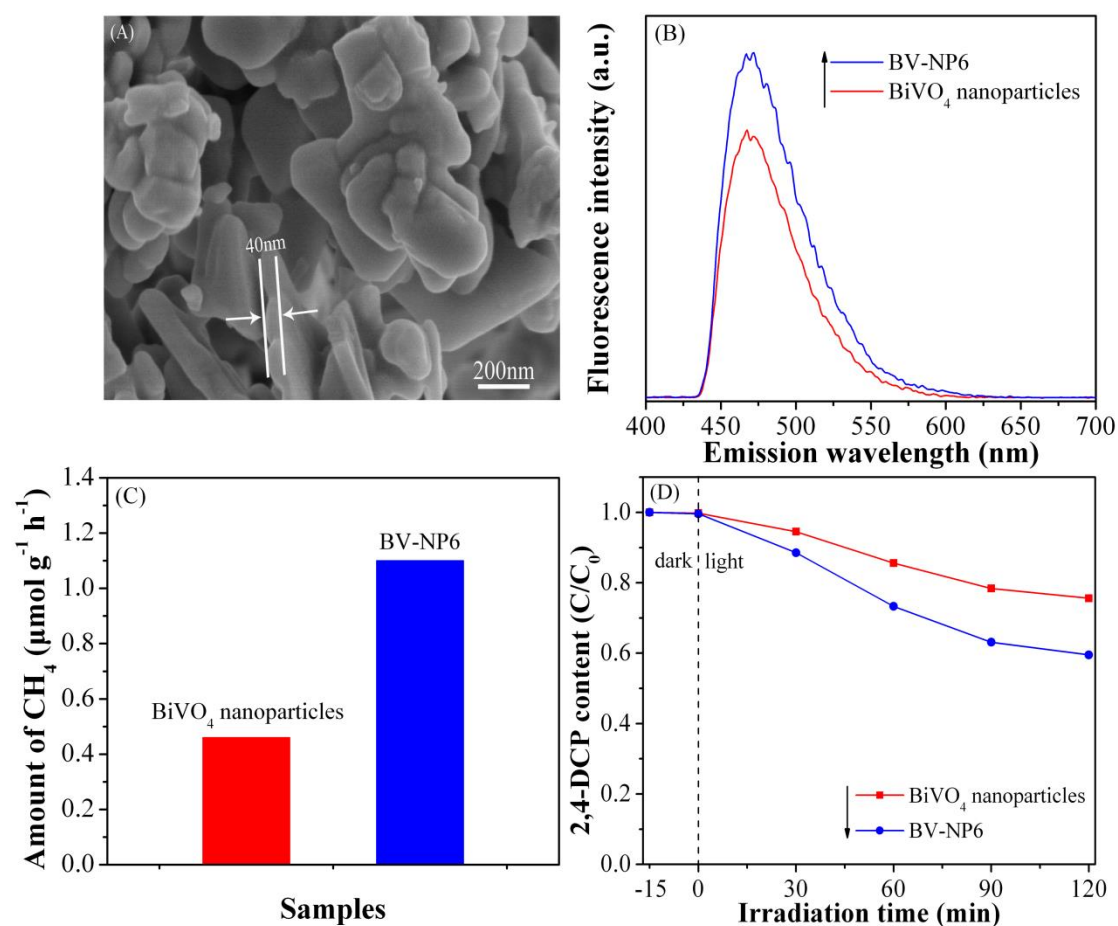


**Figure 1.** SEM image of BV-NP6 (A), fluorescence spectra of the formed hydroxyl radicals (B), CO<sub>2</sub> reduction (C) and 2,4-DCP degradation (D) under visible-light ( $\lambda > 420$  nm) irradiation of BiVO<sub>4</sub> nanoparticles and BV-NP6 (BV-NP means BiVO<sub>4</sub> nanoplates, the number 6 represents different hydrothermal time (h)).

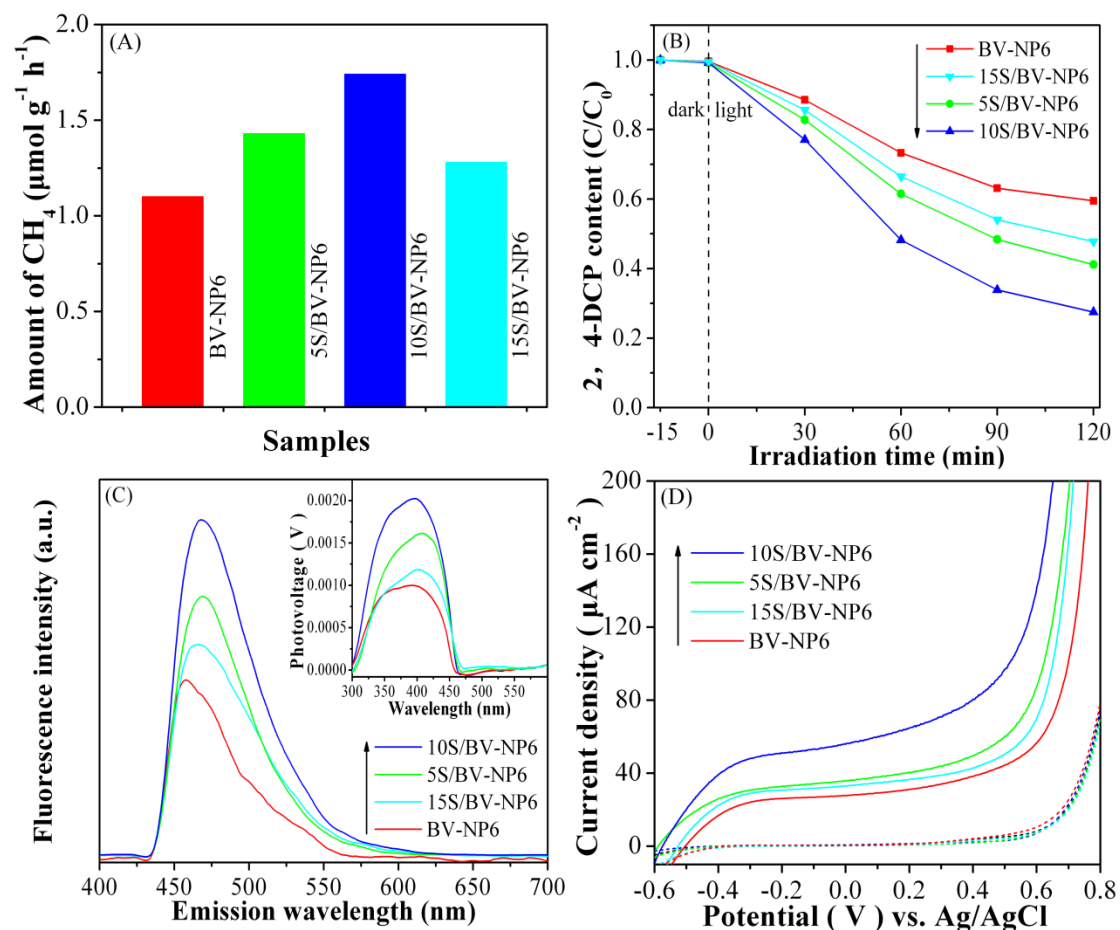


**Figure 2.**  $\text{CO}_2$  reduction (A), 2,4-DCP degradation (B), fluorescence spectra related to the formed hydroxyl radical amounts with the SS-SPS responses in the inset (C) and current density-voltage curves (D) of BV-NP6 and YS/BV-NP6 samples under visible-light ( $\lambda > 420 \text{ nm}$ ) irradiation (S means  $\text{SnO}_2$ , and Y represents the different percentage mole ratios of  $\text{SnO}_2$  coupled to  $\text{BiVO}_4$ ).

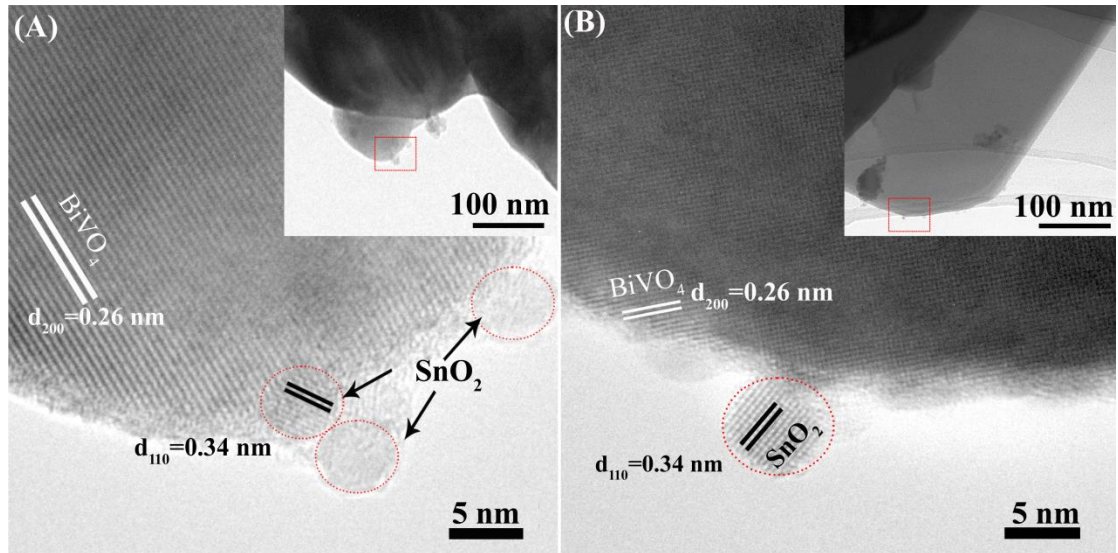


**Figure 3.** HRTEM image of 10S/BV-NP6 with the TEM image in the inset (A), HRTEM image of 5Si-10S/BV-NP6 with the TEM image in the inset (B) (Si means TEOS, and the number 5 represents the mole ratios percentage of used TEOS to SnO<sub>2</sub>).

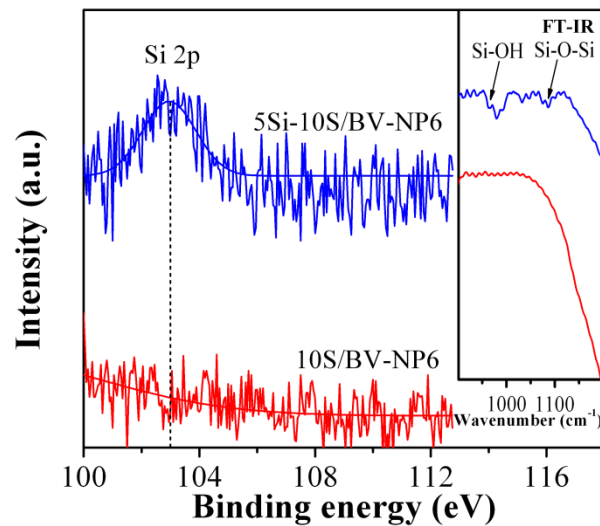


**Figure 4.** High resolution XPS spectrum of Si 2p over 10S/BV-NP6 and 5Si-10S/BV-NP6 samples with FT-IR spectra as the inset.

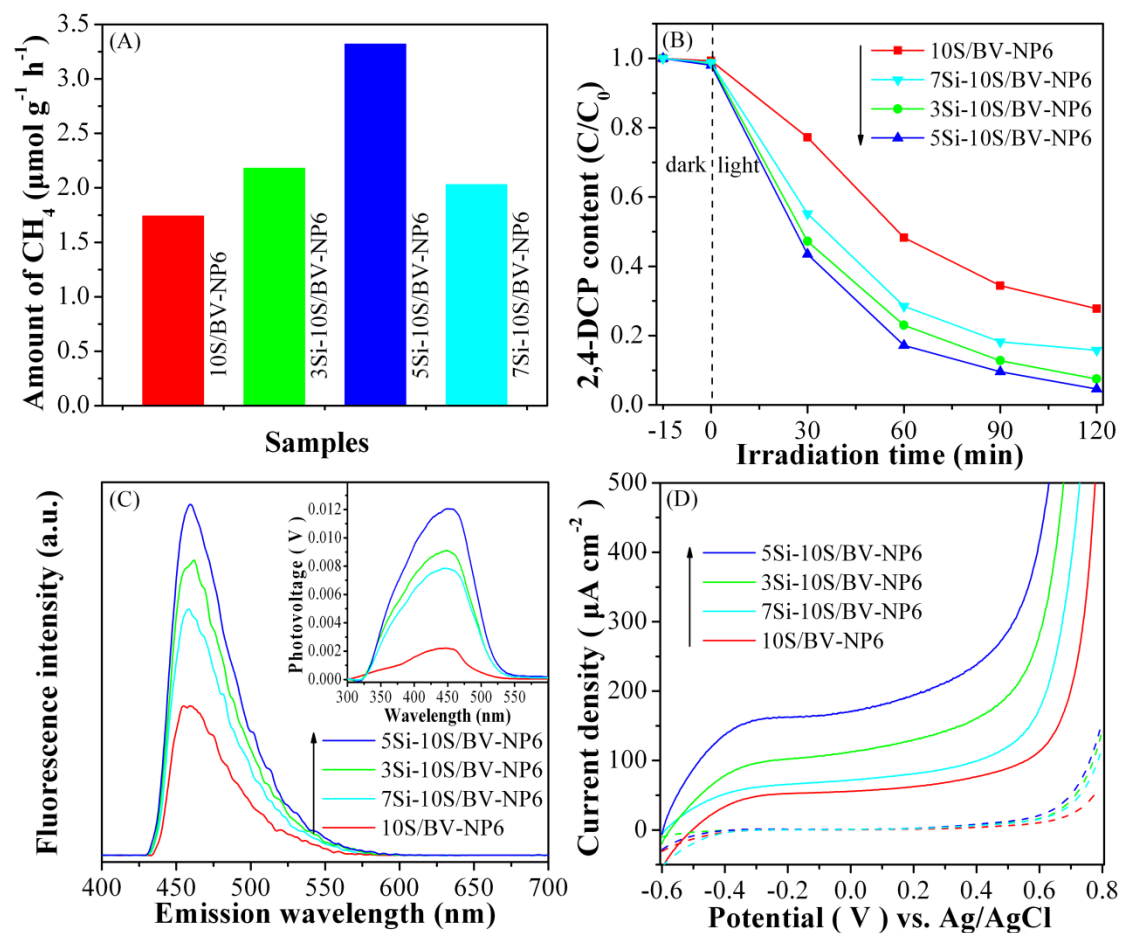


**Figure 5.**  $\text{CO}_2$  reduction (A), 2,4-DCP degradation (B), fluorescence spectra related to the formed hydroxyl radical amounts with the SS-SPS responses in the inset (C) and current density-voltage curves (D) of 10S/BV-NP6 and ZSi-10S/BV-NP6 samples under visible-light ( $\lambda > 420$  nm) irradiation (Z represents the mole ratios percentage of used TEOS to  $\text{SnO}_2$ ).

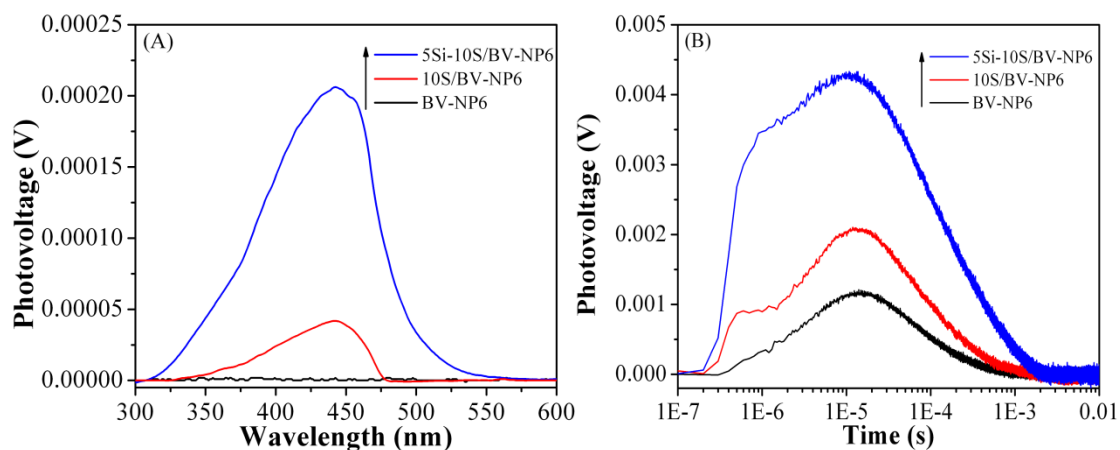


**Figure 6.** SS-SPS responses in  $N_2$  atmosphere (A) and TS-SPV responses in air (B) of BV-NP6, 10S/BV-NP6 and 5Si-10S/BV-NP6 samples.

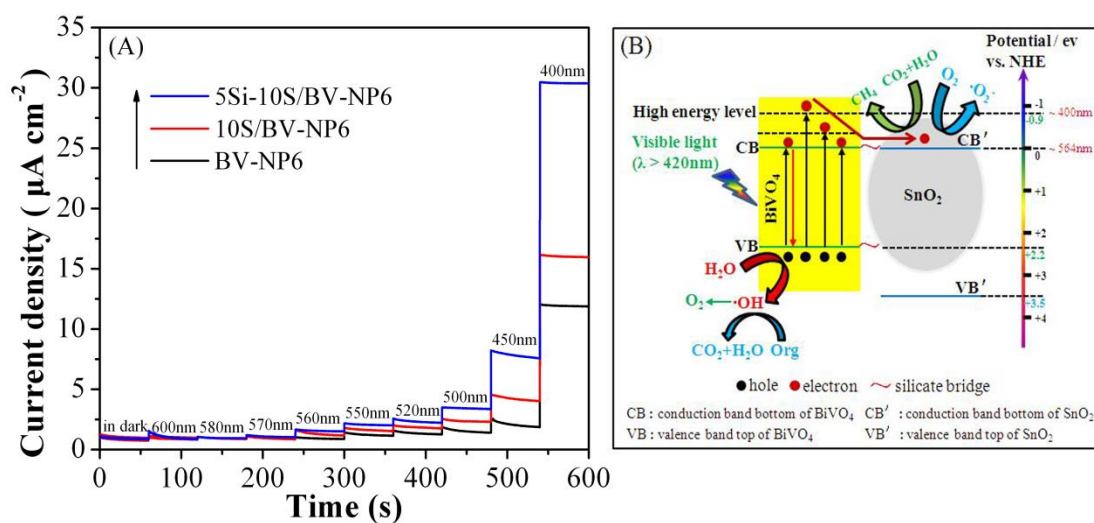
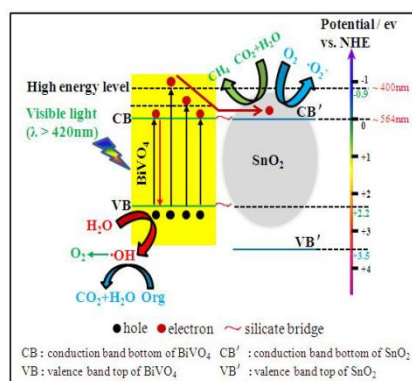


**Figure 7.** Normalized photocurrent action spectra as a function of different excitation wavelengths of BV-NP6, 10S/BV-NP6 and 5Si-10S/BV-NP6 samples (A), mechanism schematic for charge transfer and separation in  $BiVO_4$  nanoplates with silicate-bridged nano- $SnO_2$  (B).

## Graphic abstract:



Photogenerated charge separation of BiVO<sub>4</sub> nanoplates are enhanced after coupling silicate-bridged SnO<sub>2</sub>, leading to greatly improved visible-light activities for CO<sub>2</sub> conversion and 2,4-DCP decomposition.

Copyright WILEY-VCH Verlag GmbH & Co. KGaA, 69469 Weinheim, Germany,  
2013.

## Supporting Information

### **Synthesis of silicate-bridged SnO<sub>2</sub>/BiVO<sub>4</sub> nanoplate heterojunctions as efficient photocatalysts to convert CO<sub>2</sub> and degrade 2,4-dichlorophenol**

*Kang Hu<sup>1</sup>, Zhijun Li<sup>1</sup>, Shuangying Chen<sup>1</sup>, Ji Bian<sup>1</sup>, Yang Qu<sup>1</sup>, Junwang Tang<sup>2,\*</sup>,  
Liqiang Jing<sup>1,\*</sup>*

## **EXPERIMENTAL**

### **Synthesis of materials**

Synthesis of ultrathin BiOCl nanosheets. The ultrathin BiOCl nanosheets were synthesized using a modified method proposed by Xiong et al. In a typical synthesis, 0.486 g of Bi(NO<sub>3</sub>)<sub>3</sub>·5H<sub>2</sub>O and 0.400 g of PVP were dissolved in 25 mL of 0.1 mol L<sup>-1</sup> mannitol solution with vigorous stirring for 10 min. Then, 5 mL of saturated NaCl solution was slowly added into the above mixture, yielding a uniform white suspension. After stirring for 10 min, the mixture was transferred into a Teflon-lined stainless-steel autoclave of 45 mL capacity and heated at 160 °C for 3 h. After cooling to room temperature naturally, the resulting solid powders were collected by centrifugation and washed with deionized water several times to remove residual ions. The final product was then dried at 60 °C for 6 h for further characterization.

Synthesis of BiVO<sub>4</sub> nanoparticles. In a typical experiment, Bi(NO<sub>3</sub>)<sub>3</sub>·5H<sub>2</sub>O (0.01

mol) was dissolved in HNO<sub>3</sub> solution (100 mL 2.0 mol L<sup>-1</sup>) under vigorous stirring at room temperature. Subsequently, PEG (1.0 g) and NH<sub>4</sub>VO<sub>3</sub> (0.01 mol) were added into the above mixture and pH was adjusted to 7.0 with the help of 1.0 mol L<sup>-1</sup> NH<sub>3</sub>·H<sub>2</sub>O solution. The resulting mixture was kept under continuous stirring for 1 h and then ultrasonicated for 30 min. At last, the solution was centrifuged and washed with distilled water and absolute ethanol in turn, and then dried at 60 °C in air. BiVO<sub>4</sub> nanoparticles were obtained after calcination at 450 °C for 2 h in air.

Preparation of thin films for PEC measurements. The corresponding paste was prepared in advance as follows: synthesized nanocomposite powder (0.1 g) was dispersed in isopropyl alcohol (1.0 mL), and then treated by an ultrasonic process for 30 min and stirring for 30 min. Macrogl-6000 (0.05 g) was then added to the system, and re-treated by an ultrasonic process for 30 min and stirring for 30 min. At last, acetyl acetone (0.1 mL) was introduced to the above mixture, followed by an ultrasonic treatment and continuously stirring for 72 h. Conductive fluorine-doped tin oxide (FTO)-coated glasses was used as the substrates for the nanocomposite films. Prior to use, glasses were cleaned by sonicating in acetone for 30 min and then in deionized water for another 30 min. After drying in air for 10 min, the cleaned FTO glasses were sintered at 450 °C for 30 min prior to use. Nanocomposite films were prepared by the doctor blade method using Scotch tape as the spacer. Following drying in air for 10 min, films were sintered at 450 °C for 30 min. When the temperature returned to room temperature, the FTO glass covered by the nanocomposite film was cut into approximately 1.0 cm × 3.0 cm pieces with a

nanocomposite film surface area of 1.0 cm × 1.0 cm. To make a photoelectrode, an electrical contact was made with FTO substrate by using silver conducting paste connected to a copper wire, which was then enclosed in a glass tube.

### **Analysis of produced hydroxyl radical amount**

0.02 g catalyst was dispersed in 50 mL coumarin aqueous solution (0.001 M). Prior to irradiation, the mixed solution was vigorously stirred in dark for 10 min to achieve an adsorption-desorption equilibrium. After 1 h irradiation by 150 W GYZ220 high-pressure xenon lamp, the solution was centrifuged and a certain volume of supernate was transferred into a Pyrex glass cell for the fluorescence measurement of 7-hydroxycoumarin at 332 nm excitation and 460 nm emission wavelengths through a spectrofluorometer (Perkin-Elmer LS55).

### **PEC measurements**

PEC measurements for samples was performed in a glass cell using a xenon lamp (500 W), with a monochromator (CM110, Spectral Products) and a stabilized current power supply as the illumination source and an aqueous solution of NaOH (1.0 mol L<sup>-1</sup>) as electrolyte. The working electrode was the testing film (illumination area about 1.0 cm<sup>2</sup>), illuminated from the FTO glass side. Platinum wire (99.9 %) was used as the counter electrode, and a saturated KCl Ag/AgCl electrode (SSE) as the reference electrode. All the potentials were referenced to SSE at 25 °C. Oxygen-free nitrogen gas was bubbled through the electrolyte before and during the experiments. Applied potentials were controlled by a commercial computer-controlled potentiostat

(AUTOLAB PG STAT 101). For comparison, the current was also measured under dark condition.

### EIS and photocurrent action spectra

EIS were conducted in a three-electrode equipped with a Electrochemical Workstation (CHI 660, Shanghai CH Instruments CO., China) and a frequency range from 0.05 to  $10^5$  Hz with amplitude of 10 mV (RMS) at the bias of 0.1 V vs. Ag/AgCl in 1.0 mol  $L^{-1}$  NaOH electrolyte, using a 300 W xenon lamp as the light source with a 420 nm cutoff filter. Photocurrent action spectra as function of different excitation wavelength ( $\lambda \leq 550$  nm) were performed with monochromatic light from a 500 W xenon lamp passing the monochromator (CM110, spectral products).

### Figures-Supporting information (S)

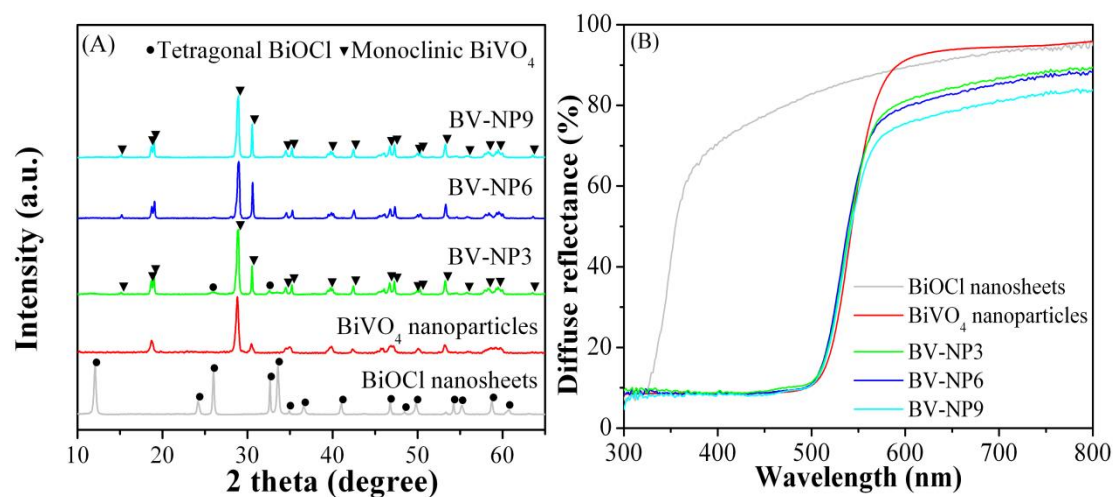


**Figure S1.** XRD patterns (A) and DRS spectra (B) of BiOCl nanosheets, BiVO<sub>4</sub> nanoparticles and BV-NPX samples (X represents different hydrothermal time).

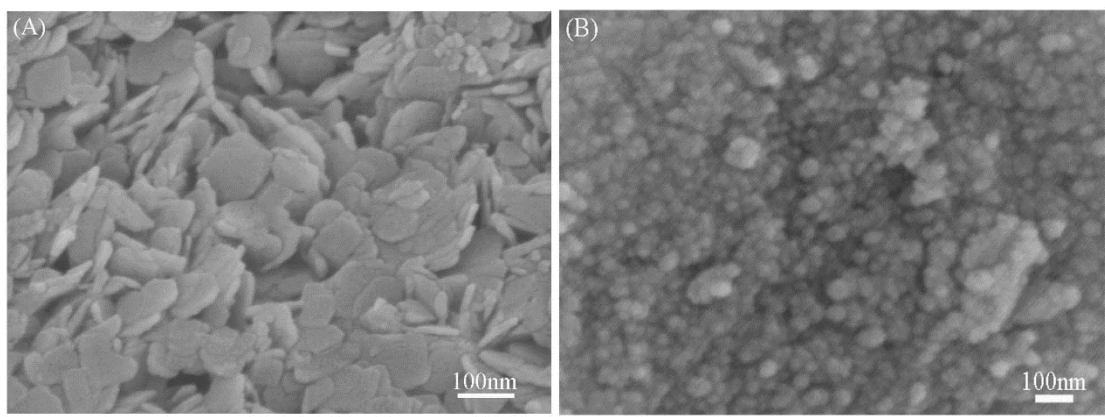


**Figure S2.** SEM images of BiOCl nanosheets (A) and BiVO<sub>4</sub> nanoparticles (B).

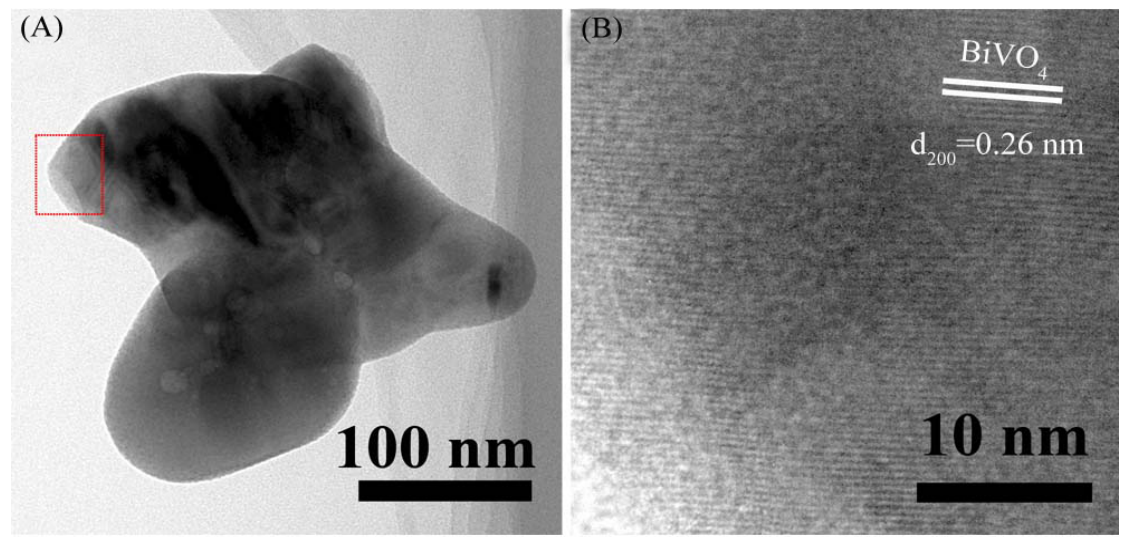


**Figure S3.** TEM image (A) and HRTEM image (B) of BV-NP6 sample.

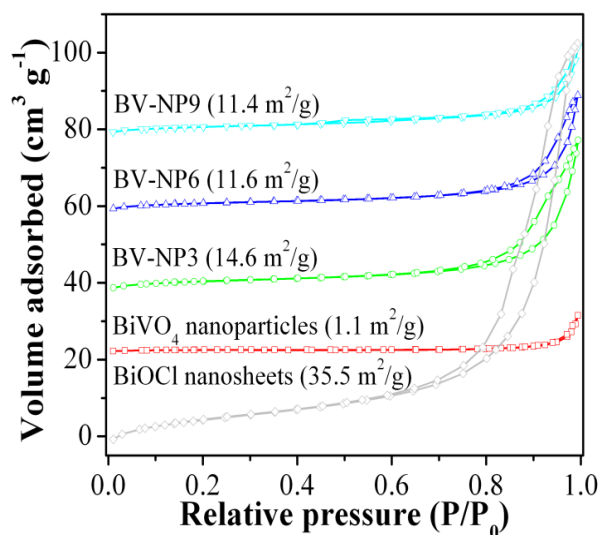


**Figure S4.** Nitrogen adsorption-desorption isotherms of BiOCl nanosheets, BiVO<sub>4</sub> nanoparticles and BV-NPX samples.

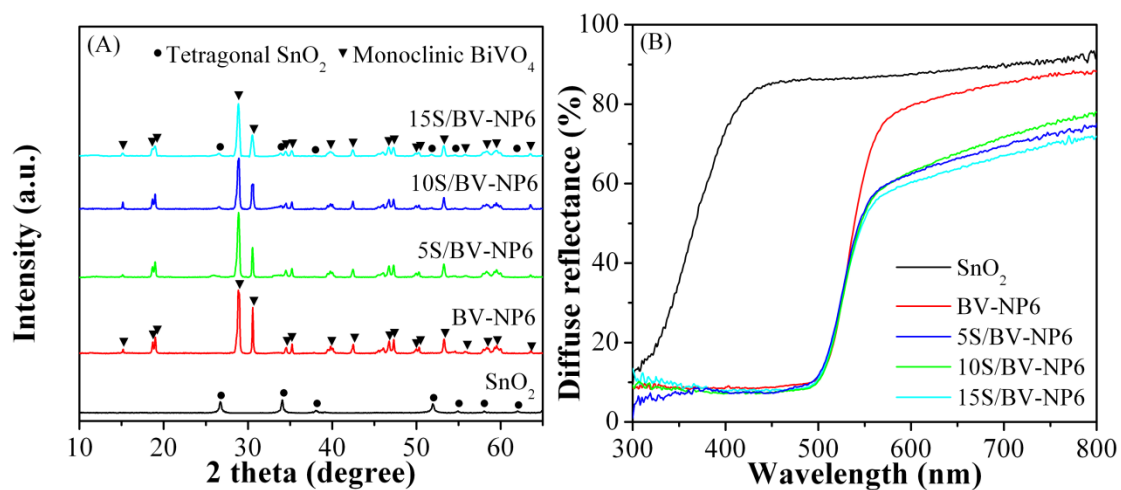


**Figure S5.** XRD patterns (A) and DRS spectra (B) of SnO<sub>2</sub>, BV-NP6, YS/BV-NP6 samples.

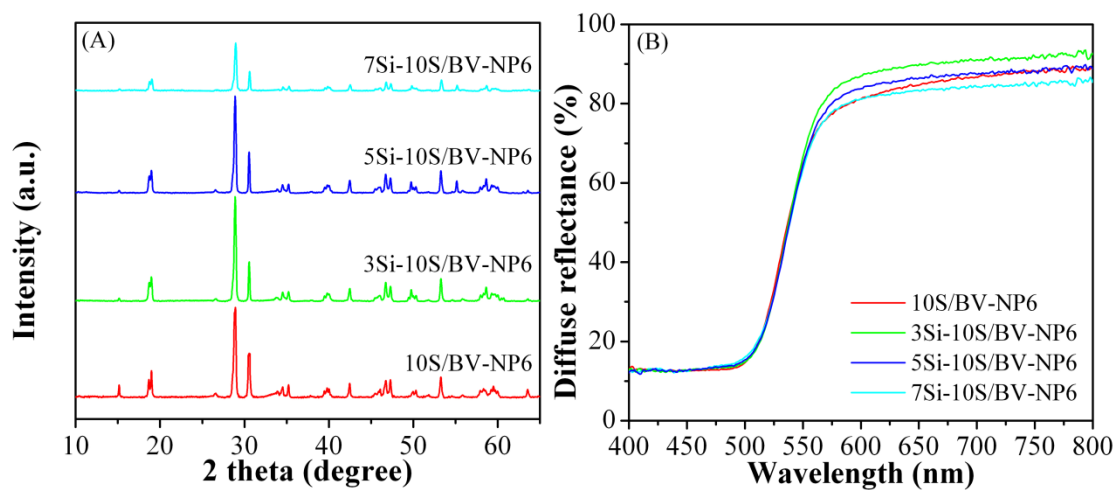


**Figure S6.** XRD patterns (A) and DRS spectra (B) of 10S/BV-NP6 and ZSi-10S/BV-NP6 samples.

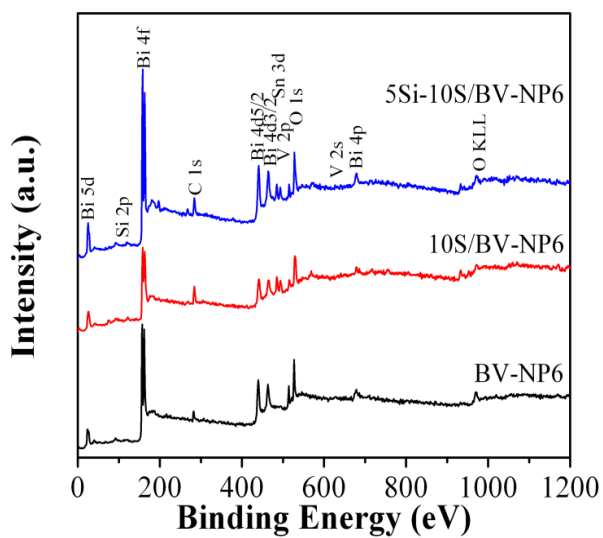


**Figure S7.** XPS survey spectra of BV-NP6, 10S/BV-NP6 and 5Si-10S/BV-NP6.

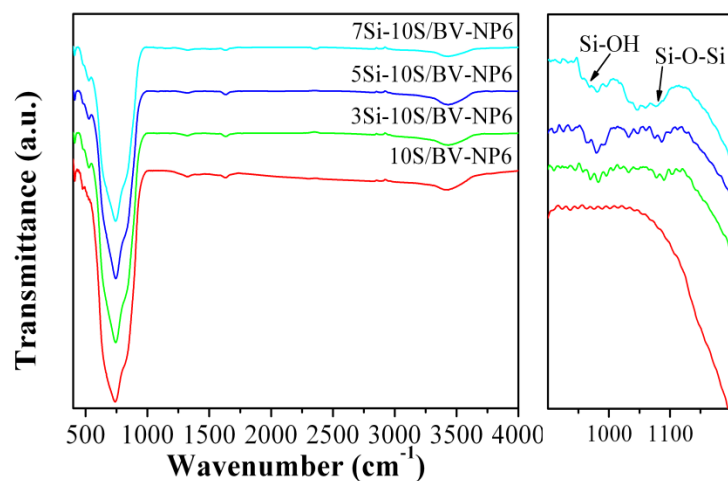


**Figure S8.** FT-IR spectra with enlarged figure as the right side of 10S/BV-NP6 and ZSi-10S/BV-NP6 samples.

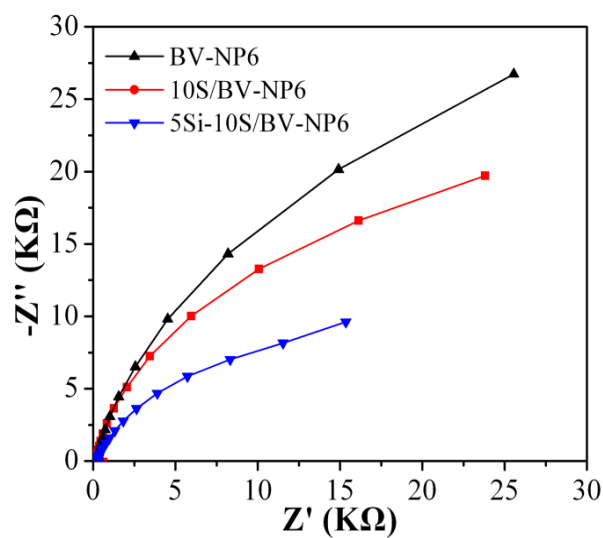


**Figure S9.** Electrochemical impedance spectra Nyquist plots of BV-NP6, 10S/BV-NP6 and 5Si-10S/BV-NP6 samples under visible irradiation.

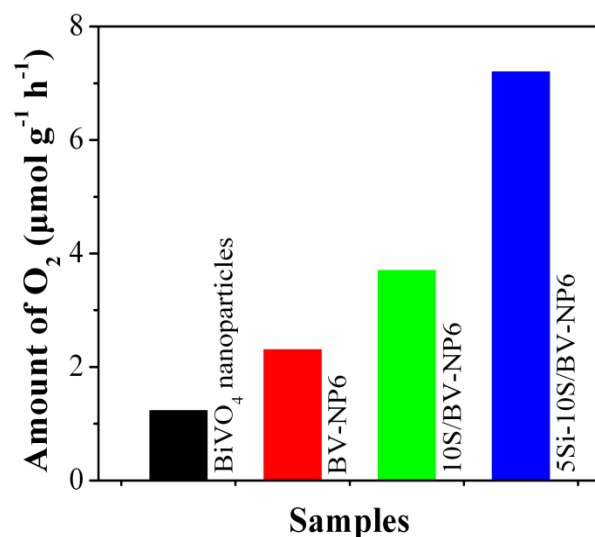


**Figure S10.** Amount of O<sub>2</sub> generated during CO<sub>2</sub> reduction over BiVO<sub>4</sub> nanoparticles, BV-NP6, 10S/BV-NP6 and 5Si-10S/BV-NP6 samples under visible-light ( $\lambda > 420$  nm) irradiation.

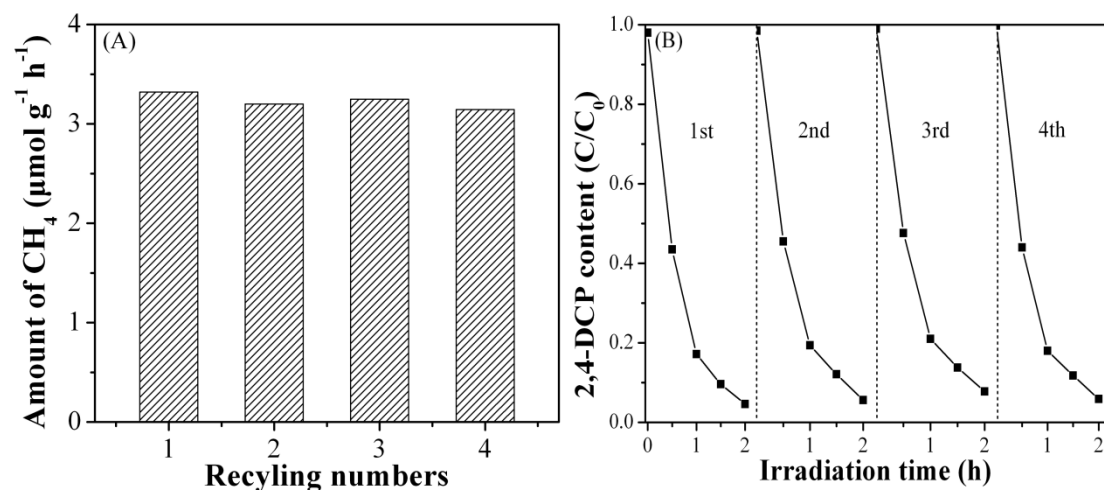


**Figure S11.** Stability tests of 5Si-10S/BV-NP6 for CO<sub>2</sub> conversion (A) and 2,4-DCP degradation (B) under visible-light ( $\lambda > 420$  nm) irradiation.

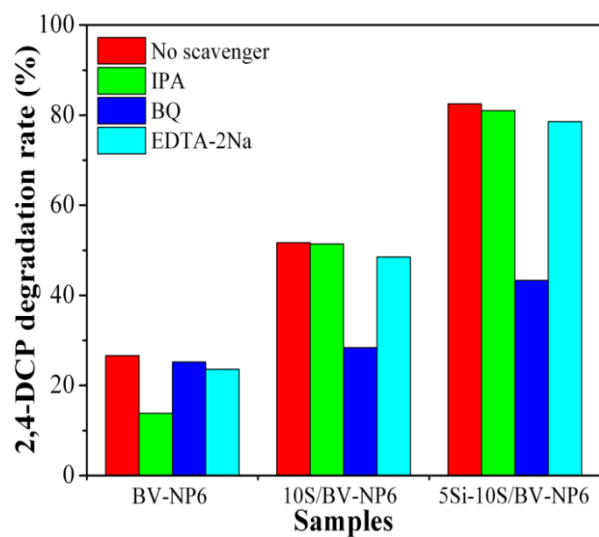


**Figure S12.** Photocatalytic degradation rates of 2,4-DCP in the presence of IPA, BQ and EDTA-2Na after visible-light ( $\lambda > 420$  nm) irradiation for 1 h over the different samples.



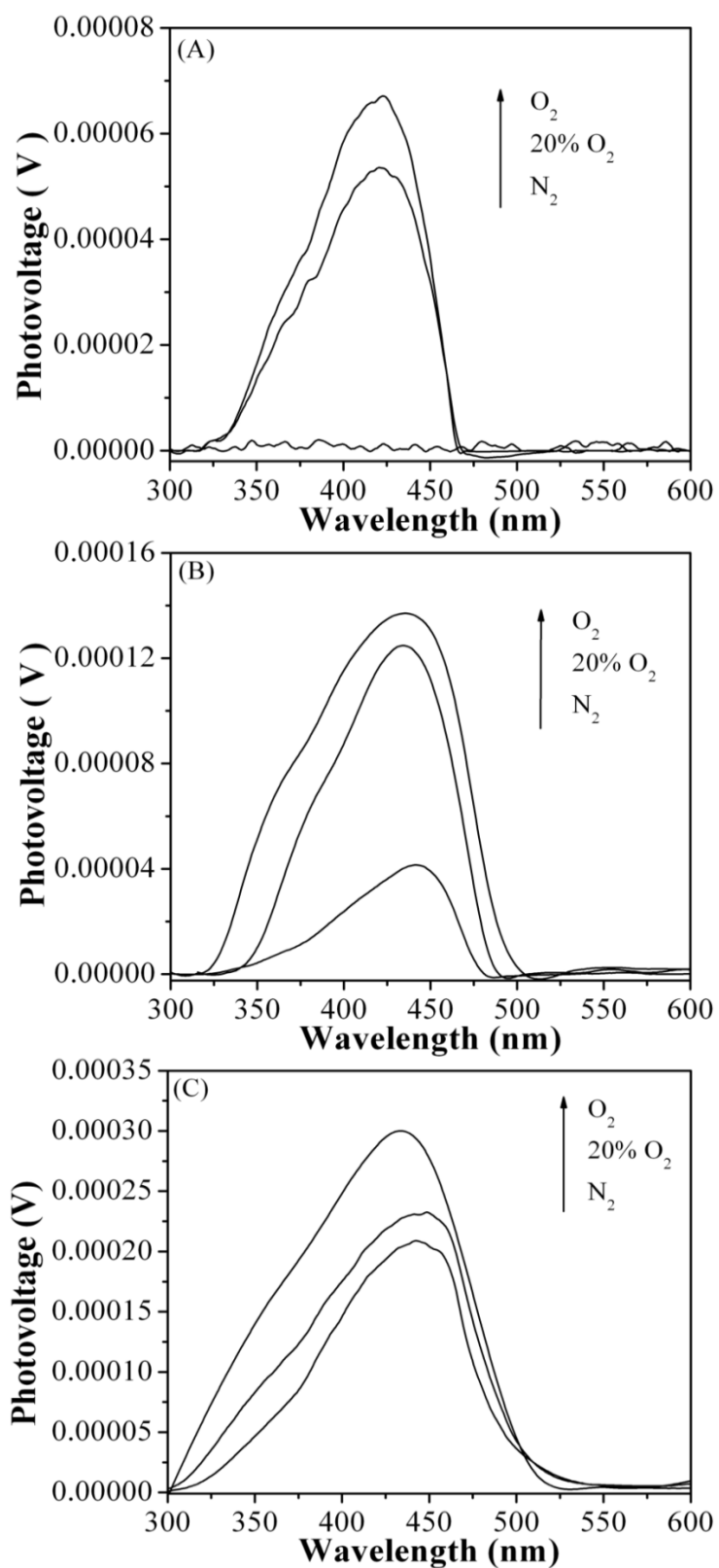


**Figure S13.** SS-SPS responses of BV-NP6 (A), 10S/BV-NP6 (B) and 5Si-10S/BV-NP6 (C) in different atmosphere.